Welding in the World
https://doi.org/10.1007/s40194-026-02490-3

RESEARCH PAPER

A comprehensive study on the optimization of laser welding process parameters for electric vehicle battery interconnections

Aygen Ahsen Yıldırım[1] · Erol Feyzullahoğlu[2] · Rıdvan Yamanoğlu[3]

Received: 15 July 2025 / Accepted: 10 May 2026
© The Author(s) 2026

Abstract
This study explored the application of laser welding for joining aluminum and Hilumin® for a cell-to-tab joints in Li-ion battery packs examining influence of laser-related parameters such as welding speed, laser power, and oscillation amplitude on the properties of welds and optimized the parameters by using Taguchi method. Initially, aluminum and Hilumin® sheet materials were joined with laser welding. Electrical resistances of the welded samples were measured. Then, lap shear strengths were determined using the tensile device. As a result of the optimizations, it was determined which laser welding parameters would result in the minimal electrical resistance and maximal joint strength. In this study, the preferred minimum electrical resistance and maximum joint strength values for battery interconnection joints, with varying laser power, welding speed, and oscillation amplitude parameters, were achieved with a combination of 890 W power, 1 mm oscillation amplitude, and 8.5 m/min speed. If optimum parameters are used in establishing the connection, the maximum weld seam strength achieved was 32.36 MPa, and the minimum electrical contact resistance was 0.4186 mΩ. Findings show that welding speed strongly influenced the microstructure and mechanical and electrical properties of the welds, with higher speeds enhancing lap shear strength and reducing electrical contact resistance by favoring ductile Fe-rich intermetallic formation, while lower speeds led to brittle Al-rich intermetallics. Increasing the welding speed also increased the strength of connection.

Keywords Laser welding · Aluminum · Hilumin® · Battery interconnections · Taguchi analysis

1 Introduction

The transportation industry contributes approximately 24% of worldwide carbon dioxide (CO_2) emissions, with nearly three-quarters from internal combustion engine vehicles [1]. To address this, emission regulations worldwide aim to reduce carbon output and mitigate climate change impacts. These regulations have increased demand for electric and hybrid vehicles (EVs and HEVs), encouraging countries to modernize their automotive sectors and lower carbon footprints [1, 2]. Given its status as the world's largest vehicle market, China's decision to prohibit the use of conventional engines has drawn greater attention to electromobility [3]. As of the 1st of March, 2019, Hainan province in China prohibited the sale of fossil fuel-powered vehicles, with the goal of achieving a complete shift to sustainable energy systems by 2030 [3].

Rechargeable batteries are crucial daily technologies, valued for renewable, sustainable, and portable energy solutions. Advances in high-energy and high-power-density battery technology are essential for automotive manufacturers working to develop fuel-efficient vehicles [4]. Electric vehicles (EVs) commonly rely on lithium-ion (Li-ion) batteries for storing energy owing to their numerous advantages, particularly their ability to store a large amount of energy and deliver strong power output [5–7]. Li-ion batteries are considered the best option for energy storage applications, especially when compared to other types like NiMH, NiCd, and lead-acid batteries, due to their superior performance. This preference stems from their advantages, including extended

Recommended for publication by Commission IV - Power Beam Processes

✉ Erol Feyzullahoğlu
efeyz@kocaeli.edu.tr

[1] Rimac Technology, Battery Process Development, Zagreb, Croatia

[2] Mechanical Engineering Department, Kocaeli University, Umuttepe Campus, İzmit 41380, Turkey

[3] Metallurgy and Materials Engineering Department, Kocaeli University, Umuttepe Campus, İzmit 41380, Turkey

lifespan, superior energy/power densities, and portability [8]. A typical Li-ion EV battery system includes numerous individual battery cells, ranging from several hundred to thousands, interconnected to deliver the necessary energy [9]. The geometries of Li-ion battery cells utilized in electric vehicles encompass cylindrical, prismatic, and pouch cells. Each geometry harbors distinct advantages and drawbacks, with the favored choice contingent upon the battery's specific application and design requisites [1, 10]. Cylindrical format Li-ion cells present numerous benefits for integration into extensive battery arrays. These advantages include inherent safety features, wide availability in bulk, comparatively high energy density, and cost-effectiveness [11].

In many cases, Li-ion cylindrical battery casings are produced from Hilumin®, a nickel-coated and diffusion-annealed steel, due to its favorable electrical conductivity and strong resistance to corrosion [10]. The tab materials are selected considering factors such as their ability to conduct electricity and heat, ease of welding, and cost-effectiveness. Common options for busbar tabs include copper (Cu), aluminum (Al), nickel (Ni), and steel with a nickel-plated interstitial-free composition (Ni-Steel). Al is widely used for busbars in battery packs due to its corrosion resistance and high electrical conductivity [2, 11]. Additionally, busbars are typically constructed from copper or aluminum, with the selection of material contingent upon various factors [12–14]. Determining the right welding technique is essential for establishing reliable connections between the various components in electric vehicle battery packs, such as the connections between electrodes and tabs, tabs and terminals, and cells themselves [15]. In order to connect several cells or interface a single cell with external components, a tab or strap must be firmly attached to the battery. Figure 1 shows an example of tab connections on cylindrical cells within a battery module using laser welding [16]. Challenges in creating these joints include the following: (1) joining materials of different types and thicknesses, particularly thin ones; (2) managing surfaces with high conductivity and reflectivity; (3) addressing potential damage such as thermal, mechanical, or vibrational effects during the joining process; and (4) ensuring the long-term durability of the joint. Reliable joining techniques and parameters are needed to meet battery manufacturing requirements while maintaining high power density and low electrical loss [2, 17].

Researchers have recognized various welding methods used in automotive battery packs, including resistance spot welding, laser beam welding (LBW), and ultrasonic welding techniques [8, 11, 18]. Of these methods, LBW is the most commonly used method for joining single battery cells [8, 19, 20]. This preference arises from LBW's advantages, such as high energy concentration, minimal heat-affected zone, fast welding speed, repeatability, adaptability, ease of integration into automated processes, and the ability to join without direct contact, among other factors [8, 21]. Laser beam welding has characteristics such as minimal heat input, minimal distortions, and exceptional flexibility. Because of these properties, laser welding is widely used in welding different materials, including aluminum alloys and steels [18, 22]. The welding of Ni-steel tabs to Al busbars or Ni-steel cell casings to Al tabs is commonly used for battery pack manufacturing. Schmidt et al. conducted a study on Ni-steel tab welding, achieving welds with excellent electrical conductivity [12]. Because laser beam welding parameters play a significant role in determining weld quality, their proper selection and control are essential to achieve the desired weld penetration and joint strength. Therefore, understanding and optimizing laser beam welding parameters are vital for achieving high-quality welds in various applications [23, 24].

Research on laser welding of materials like aluminum and steel has led to the development of different joining methods over time. However, the widespread adoption of aluminum-steel welding is hindered by the challenge of producing joints exhibiting the required mechanical characteristics to

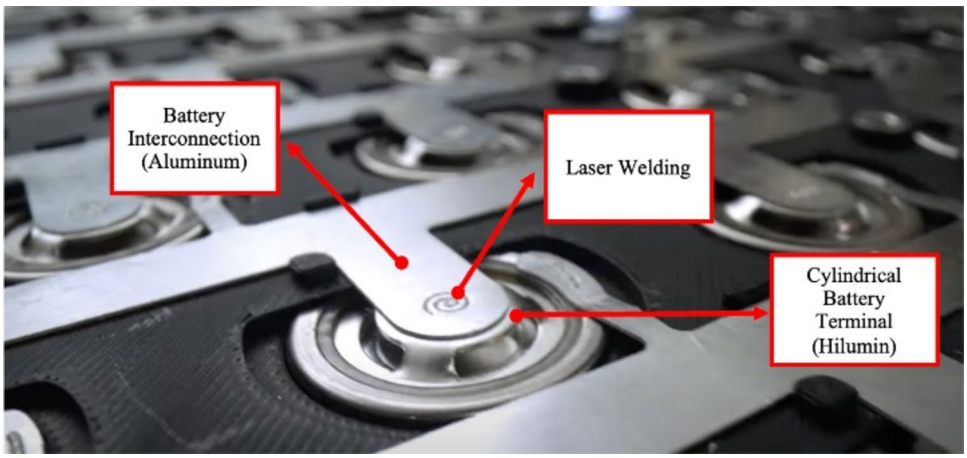


Fig. 1 Battery cell interconnects made by laser welding [16]

meet the performance requirements of specific applications. Additionally, laser welding can join complex shapes in all welding positions [25].

The Taguchi methodology provides a framework for parameter optimization, allowing efficient evaluation of factors affecting a process or product [26]. Behera employed the Taguchi method to optimize laser welding parameters for joining dissimilar materials, such as stainless steel, medium carbon steel, and 316L. The input variables included scan speed, pulse frequency, and spot size while the output variables were weld hardness and heat-affected zone (HAZ) size [23]. Pan et al. applied Taguchi methodology to refine Nd laser welding parameters for magnesium alloys, focusing on factors such as laser energy, shielding gas, and pulse frequency to maximize tensile stress [26]. Similarly, Anawa and Olabi utilized the Taguchi method in Ferritic/austenitic (F/A) joints to fine-tune variables including laser power, welding speed, and focal length, considering weld strength as the response variable [27]. Padmanaban and Balasubramanian conducted experiments to determine the best combination of process conditions for maximizing the tensile strength in AZ31B magnesium alloy. The experiments were performed based on a central composite design with complete replications. In order to enhance the tensile strength of the magnesium alloy, laser power was fine-tuned, and a mathematical model was established using response surface methodology [24].

The residual stresses induced by welding profoundly impact the weld seam's fracture strength and fatigue behavior [8, 25]. Aluminum is highly reactive and Al_2O_3 has an exceptionally high melting point of 2050 °C and is highly prone to absorbing moisture. Al_2O_3 film can obstruct the flow and fusion of liquid metals in the molten pool, potentially causing slag formation, compromising the weld joint's mechanical integrity [25, 28]. Forming Fe_xAl_y phases is essential for establishing an effective bond between the steel and the Al-alloys. Excessive formation of intermetallic phases, particularly those with a high aluminum content, can lead to increased brittleness in the welded joints [28]. Among these intermetallic compounds (IMCs), Fe_2Al_5, Fe_4Al_{13}, and $FeAl_2$ are categorized as aluminum-rich phases, while FeAl and Fe_3Al are iron-rich phases. Aluminum-rich IMCs are known by being mechanically harder and more brittle compared to the iron-rich ones. Iron-rich IMCs are preferred over aluminum-rich phases due to their lower detrimental effects and relatively higher toughness and ductility [11].

The laser welding of Fe-Al results in the formation of diverse IMC phases, each with distinct thermal expansion coefficients. These phases experience varying levels of thermal stress during the welding process, particularly during the heating and solidification stages. Consequently, thermal stresses within the weld pool may lead to the formation of cracks. Such cracking can severely affect the structural integrity of the joints, impacting their overall strength [29–31].

Ni-steel and aluminum materials are highly suitable for battery manufacturing due to their prominent physical and mechanical properties. However, welding of aluminum alloys to steel is challenging because of their limited compatibility in the course of the welding process. This phenomenon arises from the considerable variation in thermophysical characteristics, such as melting points—660 °C for aluminum alloys compared to 1538 °C for steels—as well as differences in thermal expansion, heat capacity, and thermal conductivity.Additionally, the limited ability of aluminum to dissolve in iron and the poor solubility of iron in aluminum result in the creation of fragile intermetallic compounds (IMCs) like FeAl, Fe_3Al, $FeAl_2$, $FeAl_3$, and Fe_2Al_5. These IMCs can compromise the strength of the joint. $FeAl_2$, Fe_2Al_5, and $FeAl_3$ have been recognized as Al-rich phases, whereas Fe_3Al and FeAl are considered iron-rich phases. The formation of the IMC (intermetallic compound) phases primarily relies on Gibbs free energy [32]. The swift heating and cooling cycle characteristic of laser welding act to limit the formation of intermetallic compounds (IMCs) at the weld interface while also creating a narrow heat-affected zone (HAZ). This phenomenon contributes to the production of a robust joint exhibiting improved mechanical properties [22]. Welds joining cells to tabs must have excellent electrical conductivity, mechanical durability, and thermal resilience. Nonetheless, literature highlights the difficulty in achieving robust welds when joining aluminum to steel because of the fragile nature of the intermetallic compounds (IMCs) that develop, which often results in weld failure [11].

There has been limited research on the effects of critical parameters in laser welding connections of Al and Hilumin® dissimilar materials with thin sections for battery connections. Therefore, this paper aims to investigate several crucial parameters to achieve optimal electrical contact resistance and mechanical strength in laser beam welding techniques. Laser welding speed, welding power, and oscillation amplitude parameters were selected as the variable factors. The effects of laser welding factors on the mechanical strength and electrical contact resistance of thin aluminum and Hilumin® dissimilar material joints are investigated, aiming to determine which parameter has a more significant impact on the results. Sixteen welding parameter combinations were assessed using Taguchi's method to optimize laser welding of Hilumin® and aluminum. The study systematically investigates the impact of each parameter on weld quality, considering both mechanical and electrical characteristics. Analysis of the S/N ratio identified the most effective parameters for minimal electrical resistance and maximal lap shear strength. Using Taguchi methodology, the projected optimal parameters underwent subsequent validation through microstructural, electrical, and mechanical

assessments. The main purpose of this study is to examine the laser welding performance of commonly utilized materials in battery pack manufacturing, specifically aluminum and nickel-coated steel.

2 Experimental methods

2.1 Materials used in connection of battery cells

This study selected a 0.30-mm-thick Hilumin® as the representative cell casing material and was welded to a 0.30-mm-thick tab made of 1050-grade aluminum. Table 1 provides the chemical compositions of Hilumin® and Al materials. These compositions were obtained from mill certifications. Hilumin® is a diffusion-annealed, electro-nickel-coated steel strip made from cold-rolled steel and left unpolished on both surfaces. Nickel plating is present in this material. The elemental composition does not take into account the nickel plating. Figure 2 illustrates schematic representations of lap shear joint configurations, featuring a base material size of 100 mm × 40 mm, an overlap area of 30 mm × 40 mm, and a laser-welded joint length of 30 mm. The main physical features of the materials are given in Table 2.

2.2 Production of samples with laser welding

This study used an IPG Photonics YLR-1000 Ytterbium fiber laser emitting at a wavelength of 1.07 µm for the laser welding experiments. An FLW-D30 wobble head and a 200-mm focal length focusing lens from IPG Photonics were used to direct and oscillate the multi-mode laser beam, resulting in a 100-µm spot diameter at the workpiece surface, with welding performed at the focal plane of the beam axis. A conventional circular wobble pattern was chosen to control heat input and prevent burn-through in the very thin (0.3 mm) workpiece. During the laser welding process, a conventional circular wobble pattern was applied, with a wobbling frequency of 80 Hz. This frequency was selected to ensure a homogeneous heat input and stable melt pool behavior throughout the welding process. Within the scope of the optimization study, laser welding speed, laser welding power, and oscillation amplitude process parameters were varied, while the remaining welding parameters remained unchanged. The variable parameter values were as follows: welding speed of 4, 6, 8, and 10 m/min; oscillation amplitude of 0.5, 0.8, 1, and 1.2 mm; and laser power of 850, 900, 950, and 1000 W. Before the welding process, the surfaces of the samples were carefully cleaned with IPA (isopropyl alcohol) solvent to remove contaminants like oil and dirt

Table 1 Chemical compositions of Al 1050 and Hilumin® used in welding samples (wt. %)

Al 1050	Cu	Mg	Si	Fe	Mn	Zn	Ti	Al
	0.05	0.05	0.25	0.4	0.05	0.07	0.05	Balance
Hilumin®	C	P	Si	B	Mn	S	Al	Fe
	0.044	0.010	0.002	0.0021	0.234	0.010	0.057	Balance

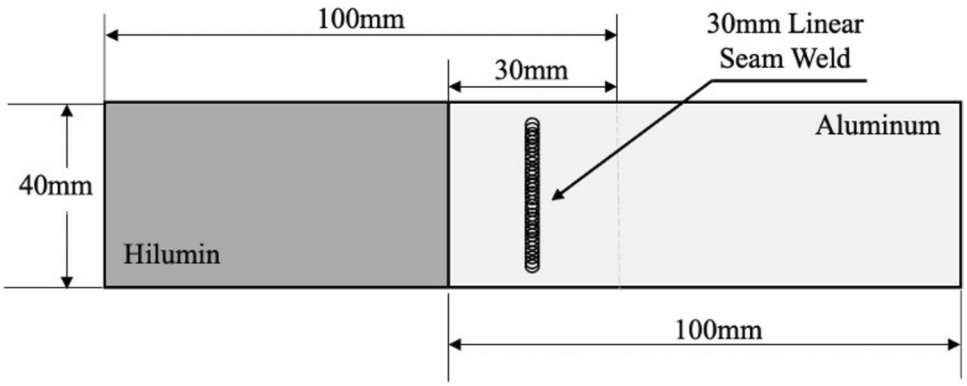


Fig. 2 The schematic of Hilumin® and Al joining sample produced by laser welding

Table 2 Physical properties of Al 1050 and Hilumin®

	Density (g/cm^3)	Electrical conductivity (S/m)	Thermal conductivity (Wm^{-1} K^{-1})	Elastic modulus (GPa)	Melting point (°C)	Boiling point (°C)
Al 1050	2.71	37.8×10^6	222	71	650	2519
Hilumin®	7.87	9.93×10^6	80	210	1536	2859

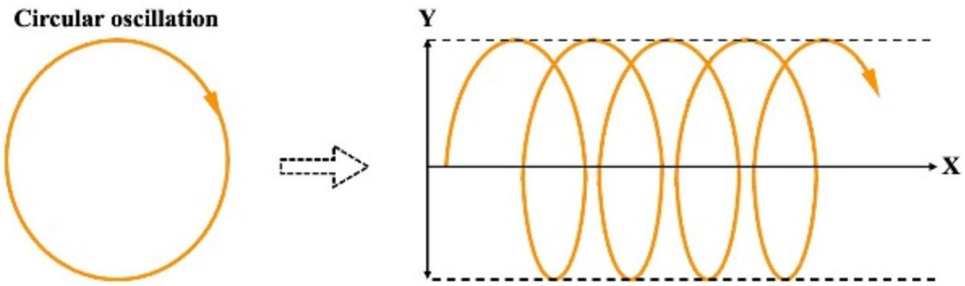


Fig. 3 The scanning path during the laser welding process

[33, 34]. In our study, linear welds with a circular oscillation pattern were used, and the weld seam was formed in a linear geometry (Fig. 3). Although circular welds are commonly used for battery connections, a single weld geometry is not universally applied. In practice, various weld geometries such as linear, arc, or C-shape can be used depending on the specific application. In the present experimental study, the used weld fixture was more suitable for producing a linear weld seam. Additionally, this geometry was chosen also by taking into account a number of studies presented in the literature on linear source geometry [2, 10, 13].

2.3 Microstructural characterization

The welded samples for microstructural investigation were sectioned at a right angle to the welding direction using the wire erosion (wire electrical discharge machining) technique. Samples were embedded in Bakelite resin and ground and polished using standard metallographic procedures. It is ground with progressively finer SiC papers, reaching a grade as fine as 2000 to eliminate scratches. Subsequently, each specimen was polished using diamond suspensions of 9, 3, and 1 µm. The samples were etched for 5 s using Keller's reagent, a mixture of 2.5 ml HNO_3, 1.5 ml HCl, 1 ml HF, and 95 ml distilled water. Microstructure examinations of the weld bead geometry were conducted using an Olympus BX41M-LED optical microscope. JEOLJSM–6060 scanning electron microscope (SEM), integrated with an energy dispersive X-ray spectroscopy (EDX) system, was utilized for the microstructural examination. Before SEM photographs were taken, the material surface was sputtered with silver for 120 s [35].

2.4 Measurement of electrical contact resistance of welded samples

In order to characterize the resistance at the welded interfaces, measurements were carried out with a 5 V GW Dual Tracking GPC-3060D Power Supply. This power supply is designed to deliver stable and reliable power to electronic devices and systems. It offers precise voltage regulation and high efficiency, making it suitable for various research, development, and testing applications. Also, a BM907 Multimeter was used, with current values of 2.5A and 5A. Resistance calculations were performed using the Ohm's law formula, which is given in Eq. (1).

$$V = I \times R \tag{1}$$

In this context, voltage (V) refers to the electrical potential difference between two points within a circuit, expressed in volts. Current (I) is the rate at which electric charge moves through a conductor, measured in amperes, whereas resistance (R) indicates how much the conductor resists this flow, measured in ohms (Ω). Measurements were conducted at 30 mm from the weld seam, with three repetitions from both material surfaces. The electrical contact resistance of welds was assessed utilizing a four-point probe technique, depicted in Fig. 4. Kumar et al. and Asirvatham et al. likewise employed the four-point probe technique to assess the electrical resistance of welded joints. In this study, the same approach was utilized to determine the electrical contact resistance [8, 11].

2.5 Lap shear tests of welded samples

Lap shear strength was evaluated using an Instron 4411 machine at a crosshead speed of 2 mm/min. In this test unit, the displacement was measured by crosshead movement. The average of three tests was used to determine the lap shear strength of the welded samples. Figure 5 displays a schematic representation of a mechanical test specimen alongside the corresponding experimental setup.

2.6 Taguchi method

The Taguchi method enables engineers to enhance product reliability and performance through resource-efficient parameter optimization [26, 36]. In this study, the focus was on three welding parameters: laser power, welding speed, and oscillation amplitude, each with four distinct levels. Parameters and their levels are given in Table 3.

In Taguchi optimization, "signal" denotes the desired or target value, while "noise" represents any undesired factors or sources of variation. The best experimental

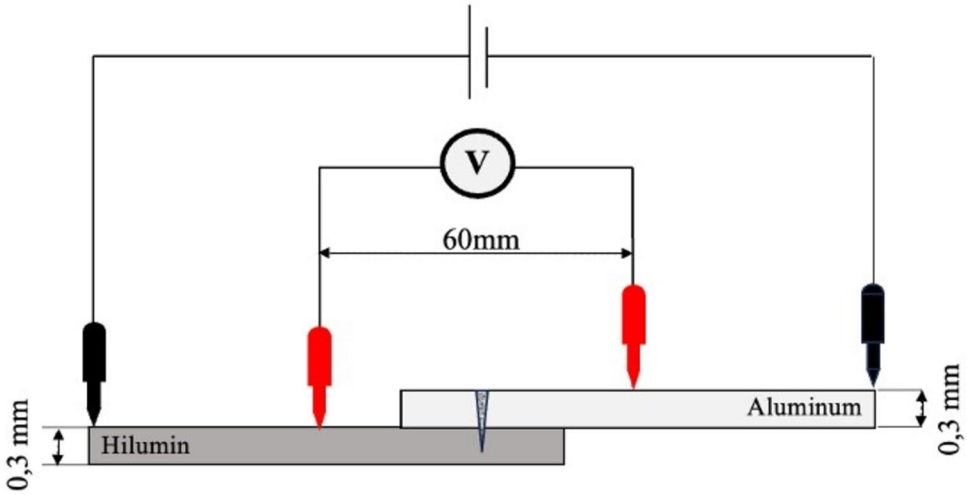


Fig. 4 Diagram illustrating the weld sample and the arrangement for measuring electrical contact resistance

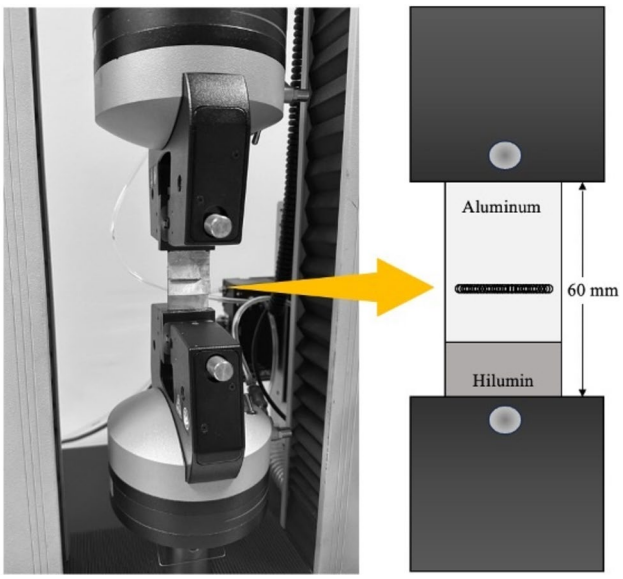


Fig. 5 Schematic representation of a lap shear test

Table 3 Process control parameters

Parameters	Unit	Level 1	Level 2	Level 3	Level 4
Laser power	W	850	900	950	1000
Welding speed	m/min	4	6	8	10
Oscillation amplitude	mm	0.5	0.8	1	1.2

outcome is determined by calculating the average signal-to-noise ratio (S/N) for each factor [36]. In battery cell interconnections, low electrical contact resistance and high mechanical strength are desired. A weld bead is defined as "better" when its electrical contact resistance is low and its mechanical strength is high. Therefore, "Smaller the better" characteristics are employed for low electrical contact resistances, while "Larger the better" characteristics are utilized for high lap shear strengths in this study. The welds were optimized for minimum electrical contact resistance and maximum lap shear strength using Taguchi optimization.

During the determination of process limits, several trial welds were conducted. Given that the maximum power capacity of the laser welding machine was 1000 W, the maximum applied power value was restricted to 1000 W for the power parameter. Below 850 W, the welding beam could not fully penetrate the material; hence, the minimum value for the power parameter was set to 850 W. Welding speeds below 4 m/min also resulted in excessive heat input, causing perforation in the base material. Upon visual inspection of the backside of the welded samples, it was noted that overpenetration occurred at welding speeds below 4 m/min. Therefore, the minimum welding speed value was set to 4 m/min, while the maximum speed value was set to 10 m/min. Oscillation amplitude reference values ranging from 0.5 to 1.2 mm were adopted for the oscillation amplitude parameter levels based on the literature [11].

An orthogonal array is a structured combination of experimental parameters. It determines the specific combinations of parameters to be tested to minimize systematic errors and achieve consistent results with minimal variation while conducting fewer experiments. For example, with three parameters, each having four levels, we would theoretically need to perform $(4 \times 4 \times 4) = 64$ experiments to optimize the parameters. However, by using an L16 orthogonal array, we can obtain similar results with only 16 carefully chosen experimental combinations [23]. Table 4 illustrates the orthogonal array with input parameters and corresponding responses. Sixteen experiments were conducted utilizing the parameters outlined in Table 4. To mitigate experimental error, each experimental set was subjected to three trials.

Table 4 Laser welding input parameters in an orthogonal array

Run order	Laser power (W)	Welding speed (m/min)	Oscillation amplitude (mm)
1	850	4	0.5
2	900	4	0.8
3	950	4	1
4	1000	4	1.2
5	850	6	0.8
6	900	6	0.5
7	950	6	1.2
8	1000	6	1
9	850	8	1
10	900	8	1.2
11	950	8	0.5
12	1000	8	0.8
13	850	10	1.2
14	900	10	1
15	950	10	0.8
16	1000	10	0.5

Table 5 The lap shear test results of aluminum–Hilumin® welded samples

Run order	Laser power (W)	Welding speed (m/min)	Oscillation amplitude (mm)	Lap shear strength (MPa)
1	850	4	0.5	11.46
2	900	4	0.8	18.04
3	950	4	1	17.72
4	1000	4	1.2	23.65
5	850	6	0.8	28.09
6	900	6	0.5	26.63
7	950	6	1.2	32.94
8	1000	6	1	26.53
9	850	8	1	28.66
10	900	8	1.2	33.82
11	950	8	0.5	27.56
12	1000	8	0.8	31.72
13	850	10	1.2	31.52
14	900	10	1	32.99
15	950	10	0.8	33.48
16	1000	10	0.5	28.32

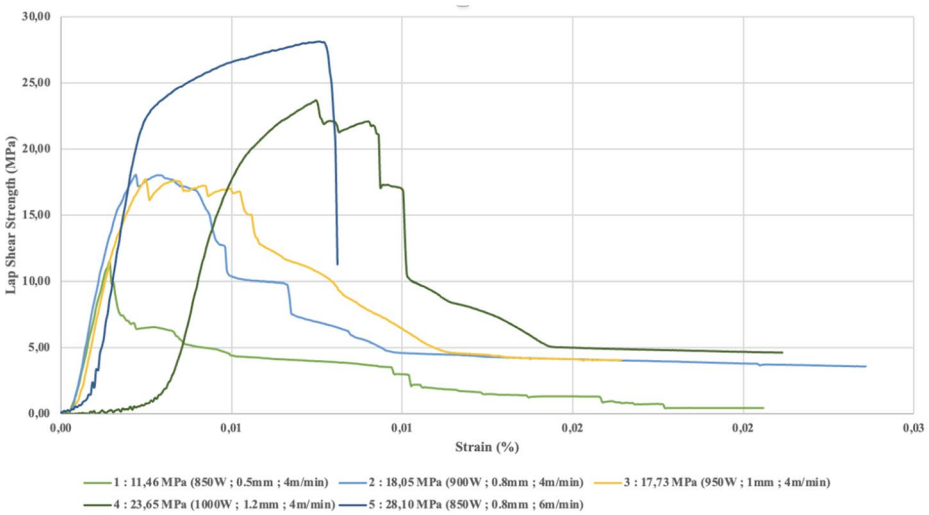
3 Results and discussions

3.1 Mechanical strength of welded samples

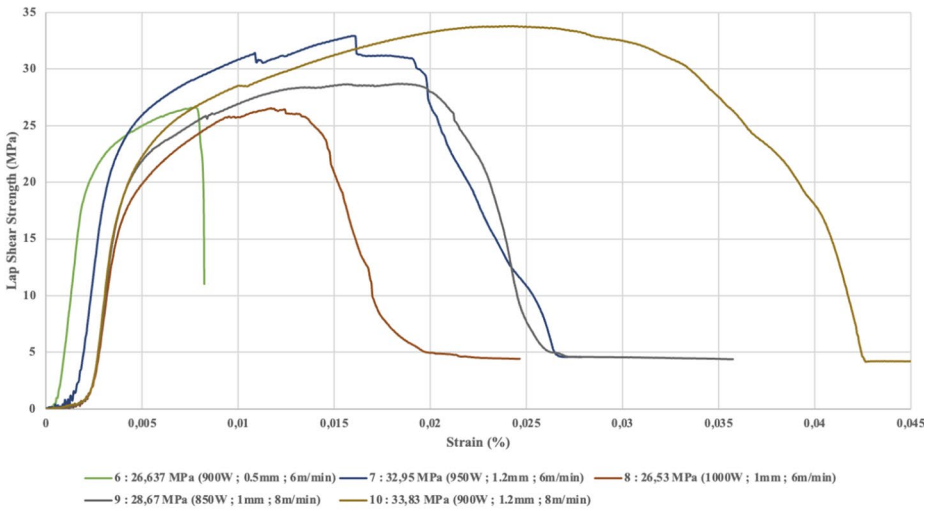
The strength of the joint plays a crucial role in determining the quality of a weld [1–8]. The lap shear test results of welded samples are presented in Table 5. The stress–strain curves of welded samples for the 16 samples are presented in three figures for clearer presentation (Fig. 6a–c). These curves establish a connection between the force exerted on a material and the resulting deformation due to that force.

The experiment results were analyzed using the Minitab program to determine how laser welding parameters affected the mechanical strength of the welded samples. According to the test results, the lap shear strength of the weld bead is expected to be high, and this is defined as "better." The lap shear test results were analyzed using Taguchi Design analysis with the criterion "the larger, the better," and signal-to-noise ratios emerged in Fig. 7. In this graph, the highest values represent the best outcomes. When ANOVA analysis was conducted on the results of Al and Hilumin® welded samples, it was determined that the parameter most influential on the lap shear strength of the welded region was "welding speed," accounting for 77.31%. According to the results of the analysis, the second influential parameter was "oscillation amplitude," with a rate of 16.18%. Among the altered parameters, it was inferred that the "laser power" factor had the least impact on the lap shear strength results, with a rate of 3.93%, shown in Table 6. Ramiarison et al. observed in their experimental study on aluminum alloy laser welding that laser power had the least effect on the sample's mechanical properties compared to oscillation amplitude and welding speed [37]. The Ramiarison et al. study correctly points out the link between weld speed and laser power in terms of specific point energy. Here, it is the combination of laser power and travel speed that produces the physical effects observed. Lower laser powers combined with lower travel speeds can produce welds of comparable strength to higher laser powers and higher travel speeds. Physical effects such as melt pool flow and laser scattering by the plume also are important. According to the analysis of this study, the results are significant for the welding speed and oscillation amplitude factors since $P < 0.05$. The R^2 value was 97.41%, indicating that the ANOVA model is reliable (Table 6). Qianqian et al. also investigated the laser welding of 1-mm-thick low carbon steel DC04 and aluminum alloy AA6016 utilizing a fiber laser. Their study aimed to examine how welding process parameters affected the weld bead's geometry and its lap shear strength. The results indicated that welding speed had the most pronounced effect on weld characteristics, whereas laser power and beam defocus had relatively less influence [38].

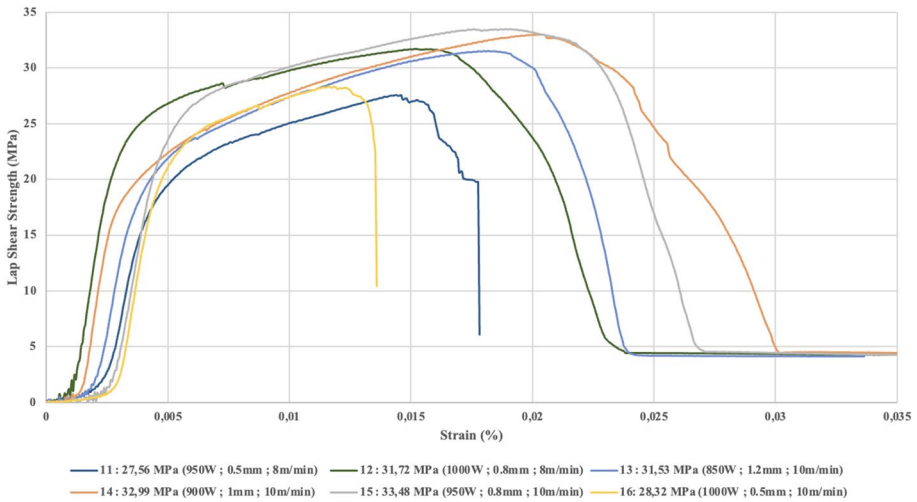
Based on the signal-to-noise analysis, the most influential parameter for aluminum and Hilumin® welded samples, "speed," reached the optimal mechanical strength at the 4th level, which is at a welding speed of 10 m/min. The increase in laser power positively affects the lap shear strength of welded samples. However, the variation between 850 and 1000 W created a very minor impact on lap shear strength of welded samples. The experimental sample, exposed to



a Stress-strain curves of welded Samples 1-5.



b Stress-strain curves of welded Samples 6-10.



c Stress-strain curves of welded Samples 11-16.

Fig. 6 **a** Stress-strain curves of welded Samples 1–5. **b** Stress-strain curves of welded Samples 6–10. **c** Stress-strain curves of welded Samples 11–16



Fig. 7 Response table for signal-to-noise ratios (larger is better)

Table 6 ANOVA results for lap shear strengths

Analysis of variance							
Source	DF	Seq SS	Contribution	Adj SS	Adj MS	*F*-value	*P*-value
Laser power [W]	3	24.63	3.93%	24.63	8.211	3.04	0.11469
Oscillation amplitude [mm]	3	101.55	16.18%	101.55	33.851	12.51	0.00542
Welding speed [m/min]	3	485.12	77.31%	485.12	161.706	59.78	0.00007
Error	6	16.23	2.59%	16.23	2.705		
Total	15	657.53	100%				
Model summary							
S	*R*-sq	*R*-sq(adj)	PRESS	*R*-sq(pred)	AICc	BIC	
1.64473	97.41%	93.53%	115.419%	81.61%	133.64	76.13	

laser welding with parameters including 900 W laser power, 1.2 mm oscillation amplitude, and 8 m/min welding speed, exhibited the highest lap shear strength of 33.82 MPa. At low laser power levels, inadequate laser penetration results in an "under-penetration" (lack of penetration). As laser power increases, penetration improves, producing an acceptable weld; however, exceeding the threshold causes excessive base material melting and over-penetration due to increased keyhole depth [8].

Figure 8 shows the cross-sectional surface of damaged weld seam after mechanical tests. Failures occurring in weld seams after lap shear tests are illustrated in Fig. 9. The main point of Fig. 9 is to show where the fracture happens. From the examination of the fractured specimens, it was observed that the upper and lower ends of the weld remain connected. Two primary failure modes can occur: interfacial failure and substrate failure. Interfacial failure happens when the lap shear strength of the weld joint is lower than that of the base plate. The welding integrity is a known ability of weld to withstand tensile, compressive, or other loads without breaking or failing. As the welding integrity increases, the fracture can occur along the weld seam, and in some cases, even the base plate can break [39]. In Fig. 9a, samples with lower lap shear strength were shown, and interfacial failure mode was observed. In Fig. 9a, the fracture occurs at the weld seam, while in Fig. 9b, it happens in the base plate. The fracture occurred in the heat-affected zone (HAZ) of base material because HAZ's strength is generally lower than that of the base metal. As depicted in Fig. 9b, it is obvious that substrate failure mode is the fracture of the base sheet along the weld seam, indicating a high welding strength, surpassing even that of the substrate's tensile strength. Figures 15, 16, 17, and 18 show the cross-sectional images with micro-scale of the fractured weld seam.

The response surface method is among the most accurate in predicting values in the welding domain compared to other

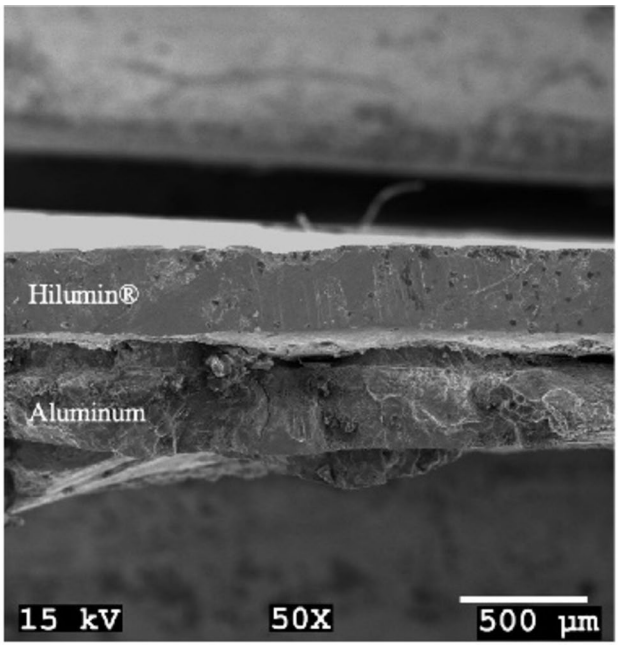


Fig. 8 The cross-sectional surface of damaged weld seam after mechanical tests

methods [37]. This method provides a map of the predicted values based on the parameters considered in the developed predictive model. The response surfaces are plotted by maintaining the value of a factor at a more favorable level for mechanical strength, as depicted in Fig. 10, which illustrates the effect of each parameter. Therefore, in Fig. 10a, the welding speed value is kept constant at 7 m/min to demonstrate the relationship between laser power and oscillation amplitude. The lap shear strength reaches high values when the oscillation amplitude is 1.2 mm, and the laser power is 900 W. In Fig. 10b, the laser power is kept constant at 925 W to illustrate the relationship between welding speed and oscillation amplitude. When the graphs prepared using the response surface method are analyzed, the maximum lap shear strength is reached when the oscillation amplitude value is 0.8 mm, and the welding speed value is 10 m/min. Figure 10c, on the other hand, shows the relationship between laser power and welding speed while keeping the oscillation amplitude constant at 0.85 mm. It was observed that the lap shear strength achieved its maximum value when the welding speed was 10 m/min and the laser power was 1000 W, highlighting the connection between these two parameters.

Figure 11 illustrates predicted values using the quadratic regression model and the experimental results. A significant relationship was noted between the experimental data and the predicted values shown in this figure. The *R*-squared (*R*^2) values for lap shear strength in the quadratic regression equations were determined to be 97.7%. The values predicted by the quadratic regression model showed greater accuracy than those from the linear regression model, demonstrating the effectiveness of the quadratic approach in forecasting lap shear strength. Although an ideal prediction would result in a perfectly straight line (indicating perfect linear correlation between predicted and measured lap shear strength), experimental data often show slight nonlinearities due to measurement variations, material behavior, and experimental conditions. The quadratic regression was applied to better capture these subtle nonlinear trends in the data. As shown in the figure, the quadratic fit provided an excellent representation of the measured values, as indicated by the high *R*^2 value (97.7%). This demonstrates that the quadratic model more accurately reflects the experimental data, accounting for small deviations that a strictly linear fit might overlook. In short, the quadratic fit is not intended to imply a fundamentally nonlinear relationship, but rather to improve the predictive accuracy and visualization of the experimental results.

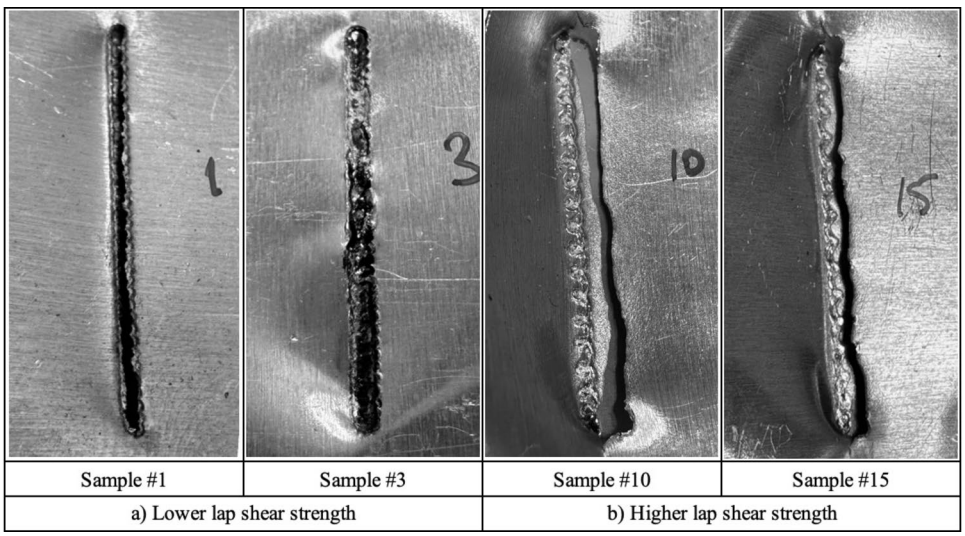


Fig. 9 Samples after lap shear tests. **a** Interface failure. **b** Substrate failure

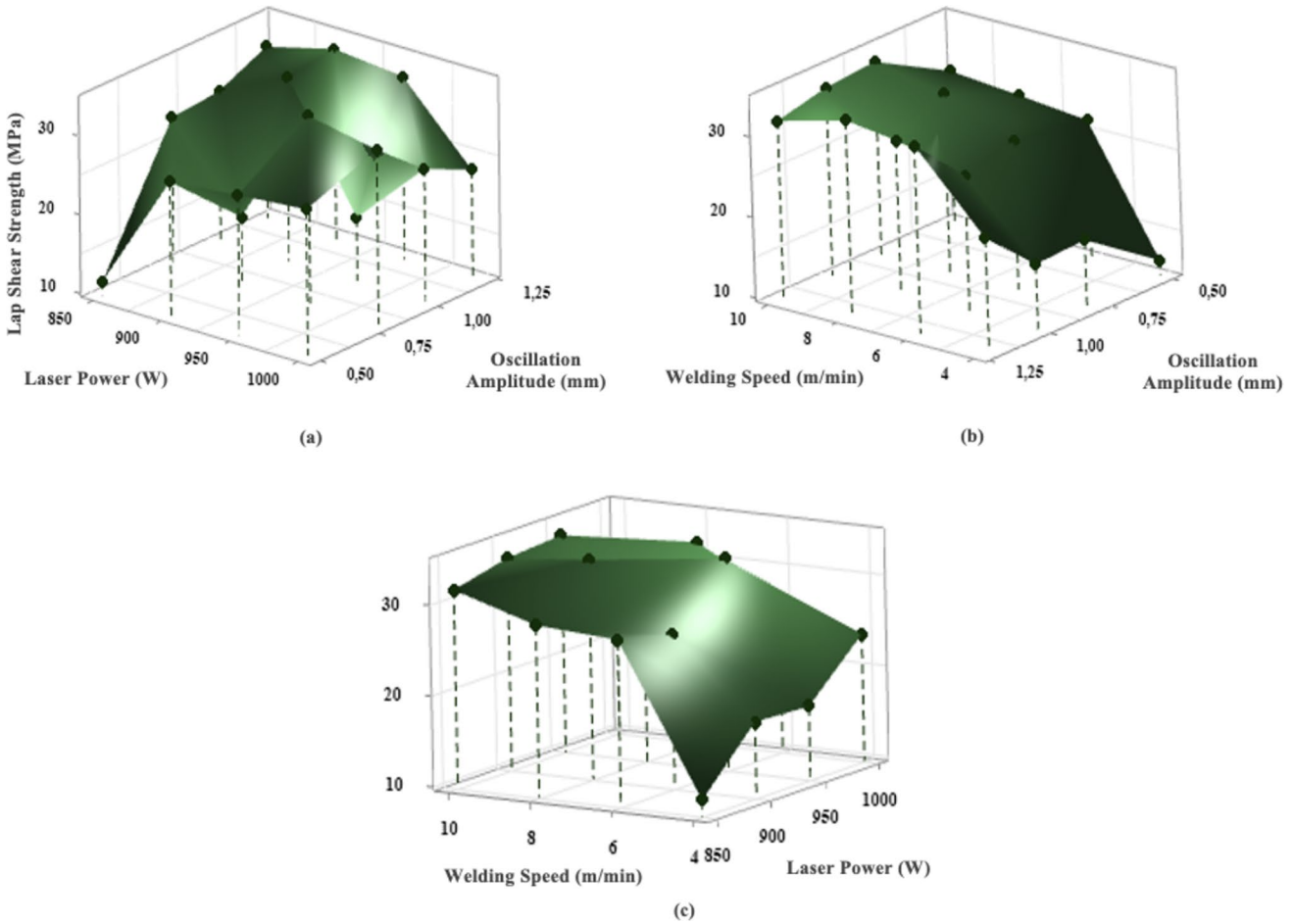


Fig. 10 Response surface graphs describing the effect of different welding parameters on lap shear strength of weld seam

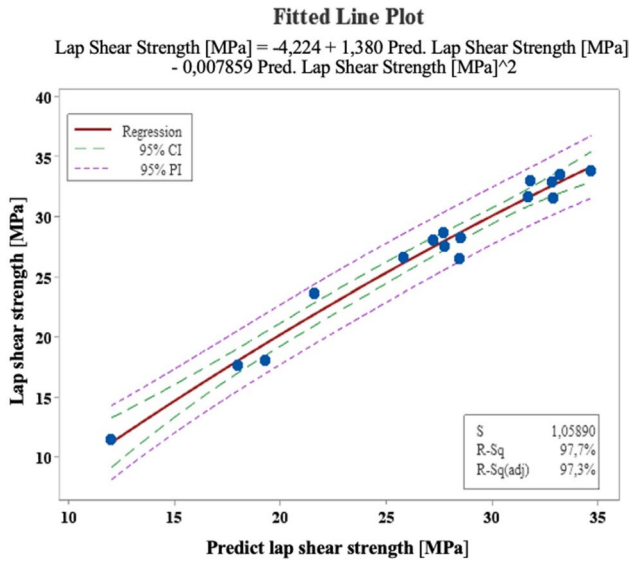


Fig. 11 Quadratic regression model compared with experimental results for lap shear strength

3.2 Electrical contact resistance of welded samples

An effective connection in an EV battery system needs to have minimal electrical contact resistance [1]. The resistance at the electrical interface was determined by measuring the voltage across the laser-welded joint using voltage probes, following the setup described in Sect. 2.4. The lowest electrical contact resistance was measured as 0.413 mΩ when the laser power was 900 W, the oscillation amplitude was 0.5 mm, and the welding speed was 6 m/min. The provided data does not directly reflect the inherent weld resistance; rather, it encompasses the total electrical contact resistance arising from the welding process and the intrinsic material resistance of aluminum and Hilumin® between the designated measuring points. As the overlapping distance was kept constant at 30 mm, any variations in the measured resistance indicate differences in the effectiveness of electrical contact made by the welds, depending on the welding parameters [11]. The electrical contact resistance results of welded samples were analyzed using Taguchi design analysis with the criterion "the smaller the better,"

and signal-to-noise ratios emerged in Fig. 12. In this figure, the highest values represent the best outcomes. When ANOVA analysis was conducted on the results of aluminum and Hilumin® welded samples, it was determined that the parameter most influential on the electrical contact resistance of the welded region was "welding speed," accounting for 83.44%. According to the results of the analysis, the second influential parameter was "laser power," with a rate of 5.9%. Among the altered parameters, it was inferred that the "oscillation amplitude" factor had the least impact on the lap shear strength results, with a rate of 1.73%, shown in Table 7. The resulting *P*-value from the analysis is less than 0.05 for the welding speed parameter. Table 7 shows that the electrical contact resistance ANOVA modeling for the aluminum and Hilumin® welding is reliable with a confidence level of 91%.

The relationships between laser power, oscillation amplitude, and welding speed parameters and their effects on electrical contact resistance are depicted in Fig. 13 as response surface plot graphs. In Fig. 13a, the welding speed value is kept constant at 7 m/min to demonstrate the relationship between laser power and oscillation amplitude. The electrical contact resistance reaches minimum values when the oscillation amplitude is 0.5 mm, and the laser power is 900 W. In Fig. 13b, the laser power is kept constant at 925 W to illustrate the relationship between welding speed and oscillation amplitude. In surface plot analysis, the minimum electrical contact resistance is reached when the oscillation amplitude value is 0.5 mm, and the welding speed value is 6 m/min. Figure 13c, on the other hand, shows the relationship between laser power and welding speed while keeping the oscillation amplitude constant at 0.85 mm. In the correlation between



Fig. 12 Response table for signal-to-noise ratios (smaller is better)

Table 7 ANOVA results for electrical contact resistance

Analysis of variance							
Source	DF	Seq SS	Contribution	Adj SS	Adj MS	*F*-value	*P*-value
Laser power [W]	3	0.000089	5.90%	0.000089	0.000030	1.32	0.352
Oscillation amplitude [mm]	3	0.000026	1.73%	0.000026	0.000009	0.39	0.766
Welding speed [m/min]	3	0.001253	83.44%	0.001253	0.000418	18.69	0.002
Error	6	0.000134	8.93%	0.000134	0.000022		
Total	15	0.001501	100.00%				
Model summary							
S	*R*-sq	*R*-sq(adj)	PRESS	*R*-sq(pred)	AICc	BIC	
0.0047258	91.07%	77.68%	0.0009529	36.52%	−53.64	−111.14	

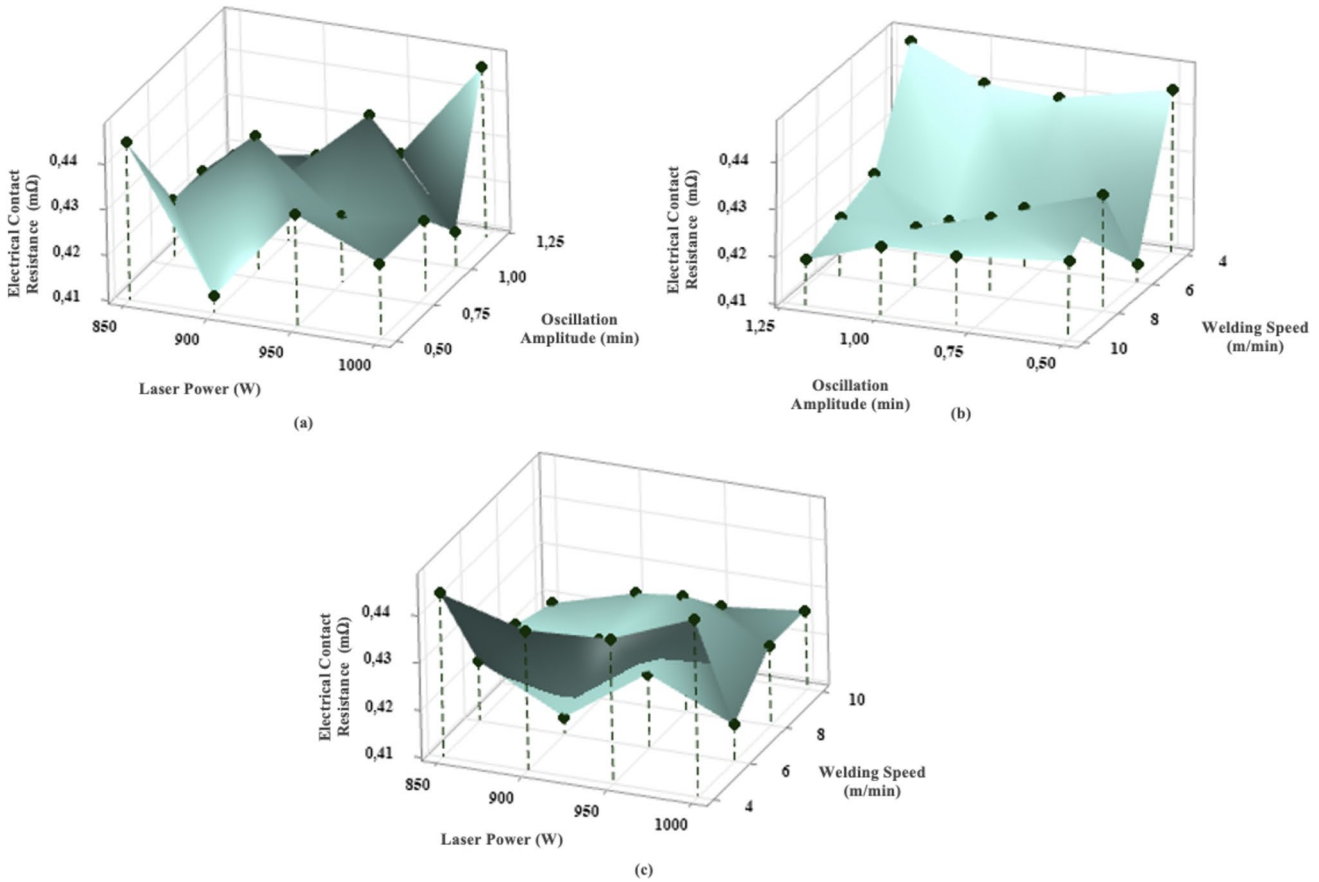


Fig. 13 Response surface graphs describing effect of the different welding parameters on electrical resistance of weld seam

welding speed and laser power, it was observed that the electrical resistance of welded samples reached its minimum value when the welding speed was 6 m/min and the laser power value was 900 W.

Figure 14 compares the predicted values obtained based on the quadratic regression analysis and the experimental results. A significant relationship was found between the predicted values and the experimental data. The *R*-squared (*R*^2) values for electrical contact resistance in the quadratic regression equations were determined to be 91.2%. The values predicted using the quadratic regression model showed greater precision compared to those from the linear regression model, demonstrating the effectiveness of the quadratic model in estimating electrical contact resistance.

Changes in the process parameters during the laser welding process affect the heat input and temperature distribution in the welded joint, leading to variations in the microstructure of the material. These microstructural changes, including phase transformations and the formation of intermetallic compounds, can influence the electrical conductivity of the material. Additionally, variations in the grain size and heterogeneity of the weld can also contribute to changes in electrical resistance. Therefore, adjustments in process

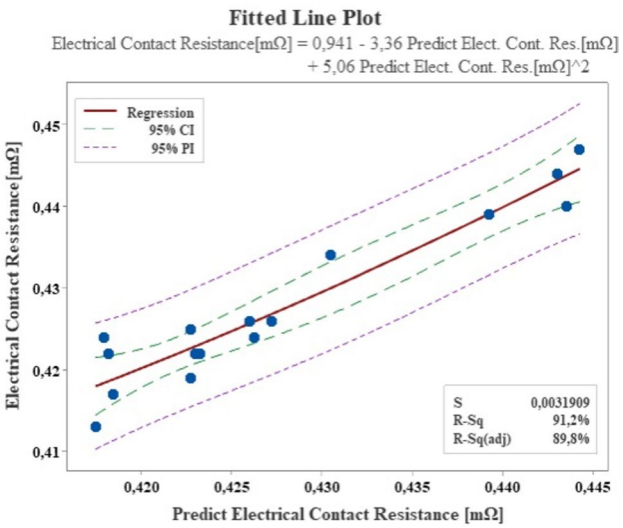


Fig. 14 Quadratic regression model compared with experimental results for electrical contact resistance

parameters, such as laser power, welding speed, and oscillation amplitude directly impact the electrical resistance due to alterations in the material's properties.

3.3 Microstructure of welded samples

The changes in process parameters affected the microstructure of the joint's cross-section. The cross-section of the welds is shown in Figs. 15 and 16. The weld seam depicted in Fig. 15 was obtained with parameters of 950 W laser power, a welding speed of 10 m/min, and a 0.8 mm oscillation amplitude, resulting in a total weld penetration depth of 180 µm. The weld seam depicted in Fig. 16 was obtained with parameters of 900 W laser power, a welding speed of 4 m/min, and a 0.8 mm oscillation amplitude, resulting in full penetration being observed, indicating an over-penetration condition. Shaikh et al. categorized weld penetration depth as "under-penetration" if it was below 0.3 times the thickness of the base material and as "over-penetration" if it was more than 0.8 times the thickness of the lower material or reached full penetration. Penetration depths falling between these values were considered optimal for a strong weld [10]. Additionally, the welding parameters illustrated in Fig. 15 produce the most favorable mechanical outcomes, whereas those depicted in Fig. 16 lead to comparatively inferior mechanical strength results.

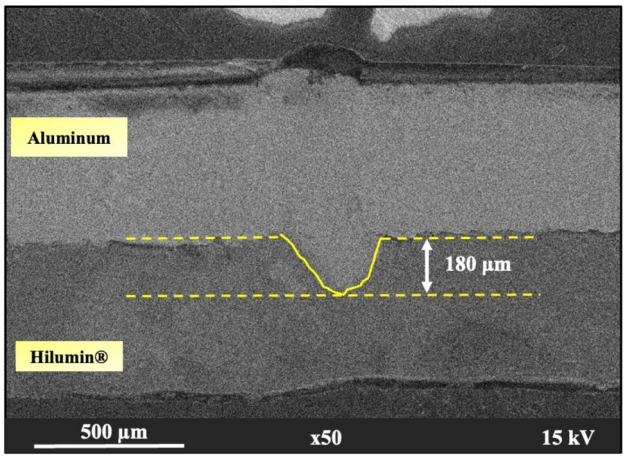


Fig. 15 Acceptable weld condition

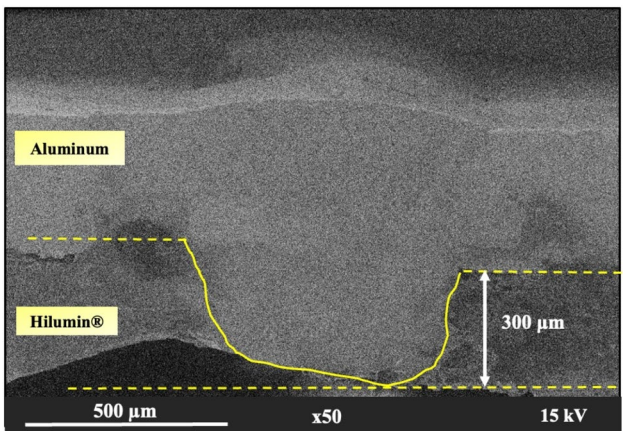


Fig. 16 Over-penetration condition

Moreover, welding steel to an aluminum alloy creates brittle intermetallic compounds (IMCs) such as $FeAl_2$, Fe_2Al_5, and $FeAl_3$ at the weld-Al interface. These IMCs adversely affect the mechanical properties of the weld joint [22]. Aluminum melts at 660 °C, whereas iron (Fe) melts at 1538 °C. Consequently, when aluminum is in a molten state, the steel base material remains solid. Once a liquid layer develops on the aluminum surface, the absorption rate of laser energy increases significantly, leading to the generation of laser-induced plasma (ionized vapor), which causes instability in the welding process. Additionally, the densities of aluminum and steel differ (aluminum is 2.69 g/cm^3, steel is 7.8 g/cm^3), and when steel melts, liquid aluminum will float on the surface of the liquid steel. This macro-scale segregation leads to poor mechanical properties of the weld joint [25]. The thermal conductivity and thermal expansion coefficient of the aluminum-steel joining differ significantly.

The fracture surfaces of the weld seam were examined following the lap shear mechanical test. Weld failures typically occur in either weld-interface mode or substrate mode. Figure 17 shows the fracture area of the laser weld for the sample exhibiting relatively weak lap shear strength (20.6 MPa), whereas Fig. 18 shows the fracture area of the laser weld for the sample with relatively high lap shear strength (32.26 MPa). In Figs. 17a and 18a, the failure surface on the aluminum side is shown. In Figs. 17b and 18b, the magnified view of the area marked with a red line can be seen. Micro-cracks can be observed on the fracture area and surfaces displaying cleavage mode failure, as depicted in Figs. 17b and 18b. When SEM images of the weld seam surface, which has relatively low lap shear strength, are examined, it is seen that there are many micro-cracks (Fig. 17).

The chemical compositions of phases present at the fracture surface of the laser weld for the specimen exhibiting relatively low lap shear strength are detailed in Fig. 19. The area chosen for analysis was chosen to be close to a region where crack formation was present, and it was aimed to emphasize the intermetallic formation in this specific zone. The intermetallic composition analyzed was identified as a Fe-Al rich intermetallic region based on the observed microstructural characteristics and local chemical composition. Chemical analysis at the location marked as No. 1 revealed 59.37 atomic% aluminum and 38.15 atomic% iron, indicating significant enrichment of Fe and Al within this zone. This compositional range is consistent with the possible formation of $FeAl_2$-dominated intermetallic phases reported in the literature for Al-steel laser welding systems. Although $FeAl_2$ is generally associated with brittle behavior, the features observed in this region reflect solidification-induced intermetallic formation during welding rather than fracture-related mechanisms.

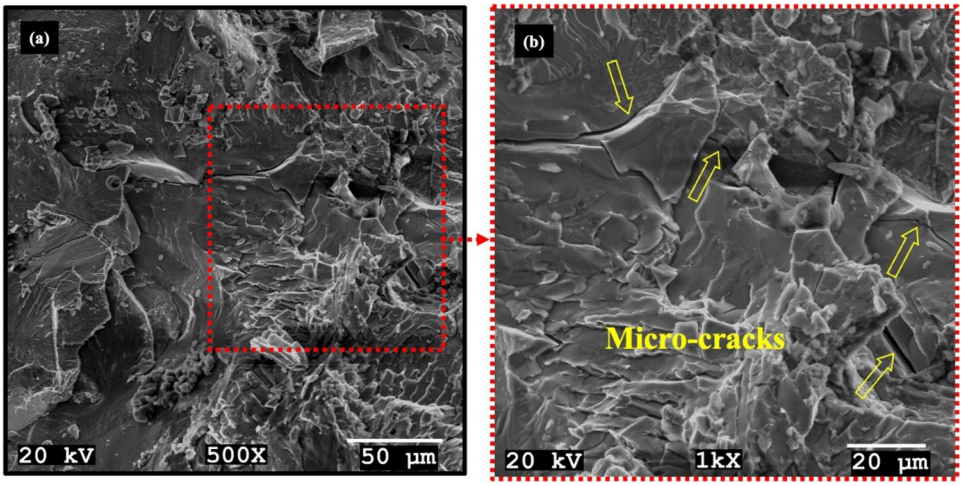


Fig. 17 Fracture surface of the laser weld for the sample with relatively low lap shear strength. **a** Failure surface at Al side. **b** Magnified view of the area marked with a red line

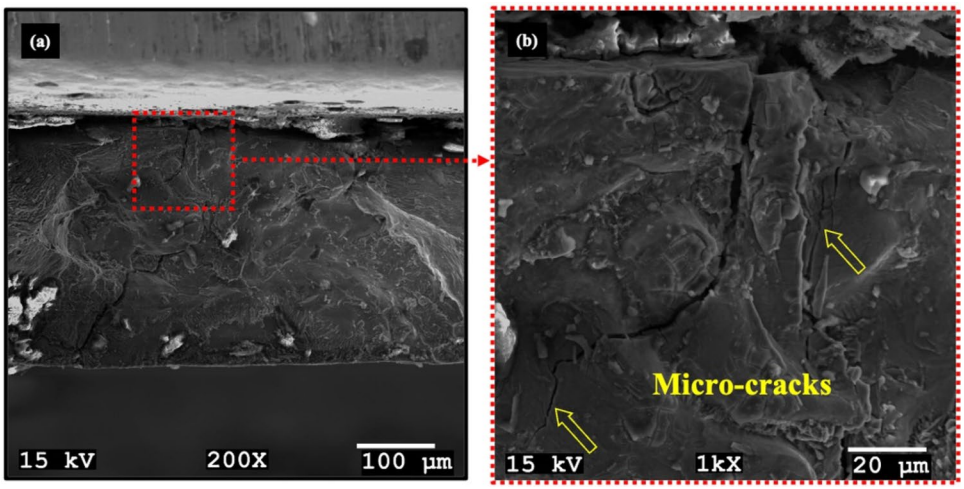
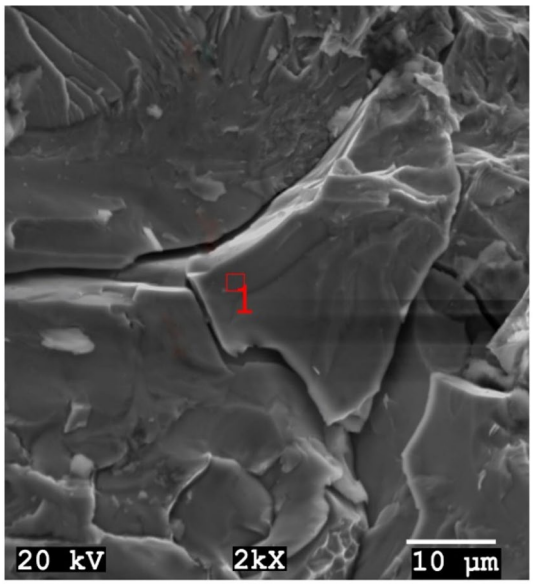


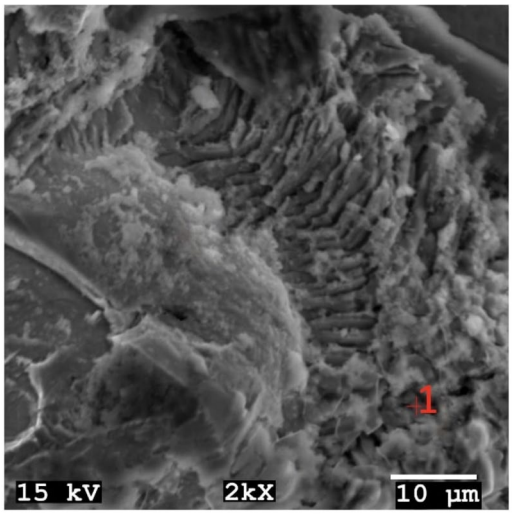
Fig. 18 Fracture surface of the laser weld for the sample with relatively high lap shear strength. **a** Failure surface at Al side. **b** Magnified view of the area marked with a red line

$FeAl_2$ is a hard and brittle intermetallic phase that reduces ductility in aluminum alloys and promotes fracture initiation. The image in Fig. 19 illustrates this situation. It was shown that the welded sample characteristics typical of brittle fracture behavior in this figure. Al-rich intermetallic compounds, such as $FeAl_2$, dominate the brittle fracture surfaces, contributing to the loss of ductility and increased susceptibility to fracture [11]. A decrease in welding speed (4 m/min) results in brittle failure at the weld seam interface. Cracks, observed on the fracture surface, are linked to the formation of brittle Fe-Al intermetallic compounds. The fracture surface of the welded sample exhibiting relatively high lap shear strength revealed a more ductile morphology characterized by plastic deformation features. This behavior is commonly associated with the dominance of Fe-rich intermetallic phases, such as Fe_3Al, which tend to form under higher welding speeds and lower specific heat input. The flow patterns arise from melt pool convection during the welding process, driven by temperature gradients and thermocapillary effects, which influence solidification behavior and result in characteristic flow-assisted morphologies. These features are observed within the weld bead and adjacent regions under conditions involving variations in laser power, welding speed, and cooling rate. The subsequent EDS analysis does reveal the presence of nickel (Fig. 20). As theoretically, the enhancement of the joint's toughness is related to the presence of AlNi compounds. Chemical composition analysis at No. 1 presented 18.79 atomic% aluminum and 71.95 atomic% iron, indicating the potential presence of the Fe_3Al intermetallic phase. Fe_3Al is known for its beneficial effects on mechanical properties of material, contributing to increased strength and ductility in welds and thus enhancing overall mechanical performance [40]. A higher welding speed (10 m/min) results in stronger, more ductile fracture behavior. The changes in process parameters affected the microstructure across the joint's cross-section by modifying the type and distribution of intermetallic phases. Specifically, lower laser speeds promoted the formation of Al-rich phases such as $FeAl_2$, leading to a brittle microstructural morphology.



Spectra	Elemental Composition, At %			Possible IMC Phase
	Al	Fe	Ni	
1	59,37	38,185	0,798	$FeAl_2$

Fig. 19 The chemical compositions of phases at the fracture area of the laser weld for the sample with relatively low lap shear strength



Spectra	Elemental Composition, At %			Possible IMC Phase
	Al	Fe	Ni	
1	18,79	71,95	4,31	Fe_3Al

Fig. 20 SEM image of the weld region used for local chemical composition analysis (EDS)

3.4 Response optimization

In Taguchi method, the Minitab Response Optimizer was used to simultaneously optimize lap shear strength and electrical contact resistance of welded samples responses and to find the balance between these responses. Verification

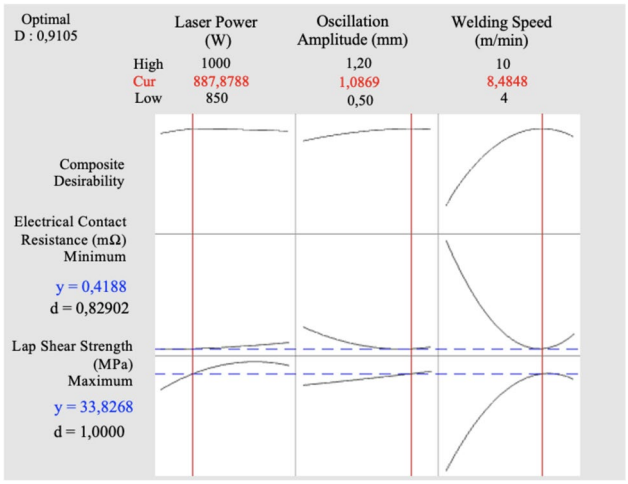


Fig. 21 Response optimizer via Minitab

experiments were conducted using these parameter values at this stage after determining the parameters that would lead to the optimal results. The main goal of the response optimization process was to maximize lap shear strength while minimizing electrical contact resistance. The laser welding was performed using a laser power value of 890 W, an oscillation amplitude of 1 mm, and a welding speed of 8.5 m/min. The optimal parameter values obtained through the Response Optimizer using the Minitab program are illustrated in Fig. 21. When the welding process was performed with these parameter values, the predicted lap shear strength was 33.82 MPa, while the electrical contact resistance was 0.4188 mΩ. After conducting the welding process with the verification parameter values, the lap shear test and electrical contact resistance measurement experiments were repeated. The electrical contact resistance was measured at 0.4186 mΩ, and the lap shear strength was measured at 32.36 MPa. It was found that the actual measurement results were highly consistent with the results predicted by Response Surface Optimizer in Minitab.

4 Conclusions

This study optimized the process parameters for joining 0.3-mm-thick Hilumin® material to 0.3-mm-thick aluminum material using laser welding, aiming to reach optimal mechanical strength and electrical contact resistance values. Based on the analysis and discussion provided above, the following conclusions can be inferred in this experimental study:

- Among the parameters of welding speed, laser power, and oscillation amplitude, welding speed has been the most influential parameter on the lap shear strength of the weld seam.

- It was observed that the lap shear strength of the welded seam increased with higher welding speeds at the parameters of 4, 6, 8, and 10 m/min.
- The experimental sample exhibited the highest lap shear strength of 33.82 MPa when subjected to laser welding with parameters including 900 W laser power, 1.2 mm oscillation amplitude, and 8 m/min welding speed.
- The changes in process parameters affected the microstructure across the joint's cross-section by modifying the type and distribution of intermetallic phases. Specifically, lower laser speeds promoted the formation of Al-rich phases such as $FeAl_2$, leading to a brittle microstructural morphology.
- The lowest electrical contact resistance was measured as 0.413 mΩ, obtained with a parameter combination of 900 W laser power, 0.5 mm oscillation amplitude, and 6 m/min welding speed.
- The analysis revealed that welding speed had the greatest impact on the electrical contact resistance in the welded area.
- Following optimization, minimal electrical contact resistance and maximal lap shear strength were achieved with a combination of 890 W laser power, 1 mm oscillation amplitude, and 8.5 m/min welding speed.
- In Taguchi method, the electrical contact resistance and lap shear strength values obtained from Minitab's response optimization tool were highly consistent with the results from the validation experiments. While the predicted values for joint shear strength and electrical conductivity resistance were 33.82 MPa and 0.4188 mΩ, respectively, the validation results yielded a lap shear strength of 32.36 MPa and an electrical contact resistance of 0.4186 mΩ.
- Examining the fracture surfaces of laser welds reveals that lower welding speeds contribute to brittle fractures with Al-rich intermetallics like $FeAl_2$, while higher welding speeds and lower energy result in ductile fractures with Fe-rich intermetallics such as Fe_3Al, enhancing weld strength and ductility.

The balance between these opposing effects underscores the importance of precise control and optimization of laser welding parameters to mitigate micro-crack formation while enhancing mechanical strength. Further research into the dynamics of IMC formation and their impact on laser welding outcomes will be essential for advancing the reliability and durability of laser welded structures in various engineering applications.

Acknowledgements Samples were supplied from Tata Steel-Europe and ASAŞ-Türkiye. Authors are thankful for the sample procurement and cooperation of Tata Steel-Europe and ASAŞ-Türkiye. The authors would also like to thank IPG Photonics-Eurasia for their support in manufacturing the welded samples.

Author contribution All authors contributed to the study conception and design. Material preparation, data collection, and analysis were performed by Aygen Ahsen Yıldırım, Erol Feyzullahoğlu, and Rıdvan Yamanoğlu. The first draft of the manuscript was written by Aygen Ahsen Yıldırım and Erol Feyzullahoğlu. All authors commented on previous versions of the manuscript. All authors read and approved the final manuscript.

Funding Open access funding provided by the Scientific and Technological Research Council of Türkiye (TÜBİTAK). There has been no financial support for this work.

Data availability We confirm data availability with our paper.

Declarations

Competing interests The authors declare no competing interests.

Open Access This article is licensed under a Creative Commons Attribution 4.0 International License, which permits use, sharing, adaptation, distribution and reproduction in any medium or format, as long as you give appropriate credit to the original author(s) and the source, provide a link to the Creative Commons licence, and indicate if changes were made. The images or other third party material in this article are included in the article's Creative Commons licence, unless indicated otherwise in a credit line to the material. If material is not included in the article's Creative Commons licence and your intended use is not permitted by statutory regulation or exceeds the permitted use, you will need to obtain permission directly from the copyright holder. To view a copy of this licence, visit http://creativecommons.org/licenses/by/4.0/.

References

1. Sadeghian A, Iqbal N (2022) A review on dissimilar laser welding of steel-copper, steel-aluminum, aluminum-copper, and steel-nickel for electric vehicle battery manufacturing. Opt Laser Technol 146:107595. https://doi.org/10.1016/j.optlastec.2021.107595
2. Dimatteo V, Ascari A, Fortunato A (2019) Continuous laser welding with spatial beam oscillation of dissimilar thin sheet materials (Al-Cu and Cu-Al): process optimization and characterization. J Manuf Process 44:158–165. https://doi.org/10.1016/j.jmapro.2019.06.002
3. Zwicker MFR, Moghadam M, Zhang W, Nielsen CV (2020) Automotive battery pack manufacturing–a review of battery to tab joining. J Adv Join Process 1:100017. https://doi.org/10.1016/j.jajp.2020.100017
4. Lee SS, Kim TH, Hu SJ, Cai WW, Abell JA (2010) Joining technologies for automotive lithium-ion battery manufacturing: a review. American Society of Mechanical Engineers Digital Collection 541–549. https://doi.org/10.1115/MSEC2010-34168
5. Sadeghian A, Iqbal N (2022) Blue laser welding of low thickness Ni-coated copper and mild steel for electric vehicle (EV) battery manufacturing. Opt Laser Technol 155:108415. https://doi.org/10.1016/j.optlastec.2022.108415
6. Solchenbach T, Plapper P, Cai W (2014) Electrical performance of laser braze-welded aluminum–copper interconnects. J Manuf Process 16(2):183–189. https://doi.org/10.1016/j.jmapro.2013.12.002
7. Gedicke1 J, Mehlmann B, Olowinsky A, Gillner A (2010) Laser beam welding of electrical interconnections for lithium-ion batteries. Laser Institute of America 844. https://doi.org/10.2351/1.5062125

8. Kumar N, Masters I, Das A (2021) In-depth evaluation of laser-welded similar and dissimilar material tab-to-busbar electrical interconnects for electric vehicle battery pack. J Manuf Process 70:78–96. https://doi.org/10.1016/j.jmapro.2021.08.025
9. Masomtob M, Sukondhasingha R, Becker J, Sauer DU (2017) Parametric study of spot welding between Li-ion battery cells and sheet metal connectors. Engineering Journal 21(7):457–473. https://doi.org/10.4186/ej.2017.21.7.457
10. Shaikh UF, Das A, Barai A, Masters I (2019) Electro-Thermo-Mechanical behaviours of laser joints for electric vehicle battery interconnects. Electric Vehicles International Conference & Show, Bucuresti, Romania
11. Asirvatham MC, Collins S, Masters I (2022) Laser wobble welding of steel to aluminium busbar joints for Li-ion battery packs. Opt Laser Technol 151:108000. https://doi.org/10.1016/j.optlastec.2022.108000
12. Schmidt PA, Schmitz P, Zaeh MF (2016) Laser beam welding of electrical contacts for the application in stationary energy storage devices. J Laser Appl. https://doi.org/10.2351/1.4943908
13. Dhara S, Finuf M, Zediker M, Masters I, Barai A, Das A (2023) Utilising blue laser over infrared laser to enhance control of penetration depth and weld strength for producing electric vehicle battery interconnects. Journal of Materials Processing Technology 317:117989. https://doi.org/10.1016/j.jmatprotec.2023.117989
14. Kick MK, Habedank JB, Heilmeier J, Zaeh MF (2020) Contacting of 18650 lithium-ion batteries and copper bus bars using pulsed green laser radiation. Procedia CIRP 94:577–581. https://doi.org/10.1016/j.procir.2020.09.079
15. Rikka VR, Sahu SR, Roy A, Jana SN, Sivaprahasam D, Prakash R, Gopalan R, Sundararajan G (2020) Tailoring micro resistance spot welding parameters for joining nickel tab to inner aluminium casing in a cylindrical lithium ion cell and its influence on the electrochemical performance. J Manuf Process 49:463–471. https://doi.org/10.1016/j.jmapro.2019.12.014
16. Fraser A (2024) The challenges of laser welding batteries. https://www.laserax.com/blog/challenges-laser-welding-batteries. Accessed 1 Jul 2025
17. Das A, Li D, Williams D, Greenwood D (2018) Joining technologies for automotive battery systems manufacturing. World Electric Vehicle Journal 9:22. https://doi.org/10.3390/wevj9020022
18. Indhu R, Divya S, Tak M, Soundarapandian S (2018) Microstructure development in pulsed laser welding of dual phase steel to aluminium alloy. Procedia Manuf 26:495–502. https://doi.org/10.1016/j.promfg.2018.07.058
19. Chen S, Huang J, Xia J, Zhang H, Zhao X (2013) Microstructural characteristics of a stainless steel/copper dissimilar joint made by laser welding. The Minerals, Metals & Materials Society and ASM International 44A:3690. https://doi.org/10.1007/s11661-013-1693-z
20. Chen C (2016) Experimental strain measurement in ultrasonic welding of battery tabs. Wayne State University, Detroit, Michigan
21. Das A, Fritz R, Finuf M, Masters I (2020) Blue laser welding of multi-layered AISI 316L stainless steel micro-foils. Opt Laser Technol 132:106498. https://doi.org/10.1016/j.optlastec.2020.106498
22. Indhu R, Manish T, Vijayaraghavan L, Soundarapandian S (2020) Microstructural evolution and its effect on joint strength during laser welding of dual phase steel to aluminium alloy. J Manuf Process 58:236–248. https://doi.org/10.1016/j.jmapro.2020.08.004
23. Behera A (2020) Optimization of process parameters in laser welding of dis-similar materials. Mater Today Proc 33(8):5765–5769. https://doi.org/10.1016/j.matpr.2020.07.148
24. Padmanaban G, Balasubramanian V (2010) Optimization of laser beam welding process parameters to attain maximum tensile strength in AZ31B magnesium alloy. Opt Laser Technol 42:1253–1260. https://doi.org/10.1016/j.optlastec.2010.03.019
25. Wang P, Chen X, Pan Q, Madigan B, Long J (2016) Laser welding dissimilar materials of aluminum to steel: an overview. Int J Adv Manuf Technol 87:3081–3090. https://doi.org/10.1007/s00170-016-8725-y
26. Pan LK, Wang CC, Hsiao YC, Ho KC (2004) Optimization of Nd:YAG laser welding onto magnesium alloy via Taguchi analysis. Opt Laser Technol 37:33–42. https://doi.org/10.1016/j.optlastec.2004.02.007
27. Anawa EM, Olabi AG (2008) Optimization of tensile strength of ferritic/austenitic laser-welded components. Opt Lasers Eng 46:571–577. https://doi.org/10.1016/j.optlaseng.2008.04.014
28. Agudo L, Eyidi D, Schmaranzer CH, Arenholz E, Jank N, Bruckner J, Pyzalla AR (2007) Intermetallic Fe_xAl_y-phases in a steel/Al-alloy fusion weld. J Mater Sci 42:4205–4214. https://doi.org/10.1007/s10853-006-0644-0
29. Li T, Zhou D, Yan Y, Peng P, Liu J (2021) First-principles and experimental investigations on ductility/brittleness of intermetallic compounds and joint properties in steel/aluminum laser welding. Trans Nonferrous Met Soc China 31:2962–2977. https://doi.org/10.1016/S1003-6326(21)65706-0
30. Peyre P, Sierra G, Deschaux-Beaume F, Stuart D, Fras G (2007) Generation of aluminium–steel joints with laser-induced reactive wetting. Mater Sci Eng A 444:327–338. https://doi.org/10.1016/j.msea.2006.09.111
31. Wang Q, Leng X, Yang T, Yan J (2014) Effects of Fe Al intermetallic compounds on interfacial bonding of clad materials. Trans Nonferrous Met Soc China 24:279–284. https://doi.org/10.1016/S1003-6326(14)63058-2
32. Indhu R, Soundarapandian S, Vijayaraghavan L (2018) Yb:YAG laser welding of dual phase steel to aluminium alloy. J Mater Process Technol. https://doi.org/10.1016/j.jmatprotec.2018.05.022
33. Wall D, Boyle M (2018) Manufacturing tomorrow, new laser sources improve battery performance by enabling dissimilar metal joining. Available from : https://www.manufacturingtomorrow.com/article/2018/08/new-laser-sources-improve-battery-performance-by-enabling-dissimilar-metal-joining/1200. Accessed 1 Jul 2025
34. Laserax USA (2024) Battery laser welding machine. https://www.laserax.com/laser-welding_machines/battery-machine. Accessed 1 Jul 2025
35. University of Illinois Urbana Champaign, JEOL JSM-6060LV Low-Vacuum SEM. https://mrl.illinois.edu/facilities/equipment/jeol-jsm-6060lv-low-vacuum-sem. Accessed 1 Jul 2025
36. Canel T, Zeren M, Sınmazcelik T (2019) Laser parameters optimization of surface treating of Al 6082–T6 with Taguchi method. Opt Laser Technol 120:105714. https://doi.org/10.1016/j.optlastec.2019.105714
37. Ramiarison H, Barka N, Amira S (2022) Optimization of parameters in laser welding of aluminum alloy 5052–H32 using beam oscillation technique for mechanical performance improvement. Int J Light Mater Manuf 5:470–483. https://doi.org/10.1016/j.ijlmm.2022.05.006
38. Qianqian G, Jiangqi L, Ping Y, Shunchao J, Wenhao H, Jianxi Z (2019) Effect of steel to aluminum laser welding parameters on mechanical properties of weld beads. Opt Laser Technol 111:387–394. https://doi.org/10.1016/j.optlastec.2018.09.060
39. Wang X, Liu B, Liu W, Zhong X, Jiang Y, Liu H (2017) Investigation on the mechanism and failure mode of laser transmission spot welding using PMMA material for the automotive industry. Materials 10:22. https://doi.org/10.3390/ma10010022
40. Kattner UR, Burton BP (1993) Phase diagrams of binary iron alloys, AI-Fe (Aluminum-Iron). The Material Information Society, ASM International

Publisher's Note Springer Nature remains neutral with regard to jurisdictional claims in published maps and institutional affiliations.